

See discussions, stats, and author profiles for this publication at: <https://www.researchgate.net/publication/231699021>

# Measurements of the Reaction–Diffusion Front of Model Chemically Amplified Photoresists with Varying Photoacid Size

ARTICLE in *MACROMOLECULES* · OCTOBER 2006

Impact Factor: 5.8 · DOI: 10.1021/ma061209l

CITATIONS

27

READS

35

7 AUTHORS, INCLUDING:



**Bryan D. Vogt**

University of Akron

159 PUBLICATIONS 2,176 CITATIONS

SEE PROFILE



**Eric Lin**

National Institute of Standards and Technolo...

223 PUBLICATIONS 3,956 CITATIONS

SEE PROFILE



**Wen-Li Wu**

National Institute of Standards and Technolo...

239 PUBLICATIONS 3,013 CITATIONS

SEE PROFILE

# Measurements of the Reaction–Diffusion Front of Model Chemically Amplified Photoresists with Varying Photoacid Size<sup>||</sup>

Bryan D. Vogt,<sup>†</sup> Shuhui Kang,<sup>†</sup> Vivek M. Prabhu,<sup>\*,†</sup> Eric K. Lin,<sup>†</sup> Sushil K. Satija,<sup>‡</sup> Karen Turnquest,<sup>§</sup> and Wen-li Wu<sup>†</sup>

Polymers Division and Center for Neutron Research, National Institute of Standards and Technology, 100 Bureau Drive, Gaithersburg, Maryland 20899, and Sematech, 2706 Montopolis Drive, Austin, Texas 78741

Received May 30, 2006; Revised Manuscript Received September 11, 2006

**ABSTRACT:** Neutron reflectivity and Fourier transform infrared spectroscopy measurements are used to profile the deprotection reaction–diffusion front with nanometer resolution in a model photoresist polymer using three perfluoroalkane-based photoacid generators (PAG) with varying chain lengths. As expected, the spatial extent of the deprotection reaction front increases with decreasing PAG size. Although the total extent of deprotection increases with increasing postexposure bake time for each PAG, the reaction–diffusion of deprotection does not propagate continuously into the photoresist polymer. The form of the deprotection reaction front changes because the diffusion process is affected by the changing polymer composition. The data are well described by a reaction–diffusion model that includes a simple acid-trapping term and does not require a varying PAG diffusivity. This high-resolution profiling, together with modeling, illustrates details of the coupled diffusion and deprotection reaction processes that affect lithographic performance.

## I. Introduction

Coupled reaction–diffusion processes are commonly encountered in nature and synthetic systems.<sup>1–5</sup> The competition between reaction and diffusion can produce intricate patterns such as Liesegang rings<sup>6,7</sup> formed within gels and Turing patterns<sup>8</sup> as recently reviewed by Grzybowski et al.<sup>5</sup> Implementation of pattern formation from reaction–diffusion into technological applications has been limited by lack of spatial extent and geometrical control.<sup>5</sup> One could imagine devices (e.g., photonic) fabricated via a single step if the feature size can be controlled on the nanoscale. The emergence of a new technology platform based on reaction–diffusion for the formation of micro- and nanostructure patterned via soft lithography illustrates the power of controlled reaction–diffusion processes.<sup>5,9,10</sup>

In the microelectronics industry, control over the kinetics and spatial extent of reaction–diffusion processes is required to produce functional devices with nanometer scale feature sizes. For example, the reaction–diffusion of copper into silicon can significantly degrade device performance.<sup>11</sup> In photolithography, high-resolution imaging is performed by converting an optical image into a chemical latent image within a photoresist via a reaction–diffusion process involving a photoinitiated acid catalyst. The chemical latent image is then developed with an aqueous base solution to produce the final pattern. These imaging materials are commonly known as chemically amplified photoresists because each photogenerated acid can catalyze several hundred reactions as it diffuses through the photoresist

material during a postexposure bake; the effect of a single photon absorption is amplified.

The quality of the final patterned structures is dependent upon factors that influence either the spatial distribution of the photoacid or the spatial extent of the reaction–diffusion process. Using interferometric lithography and varying aerial image contrast, Hinsberg et al. demonstrated that the initial acid catalyst distribution, controlled through the exposure quality, significantly affects the printed feature quality.<sup>12</sup> Pawloski et al. examined measurements of lithographic patterns under a variety of imaging conditions and identified an apparent resolution limit in the final feature quality as quantified by line edge roughness.<sup>13</sup> These changes in the feature quality have been correlated with the reaction–diffusion of the photogenerated acid<sup>14–16</sup> into the unexposed regions that leads to image spreading or blurring.<sup>17,18</sup> Controlling the reaction–diffusion process remains an important strategy for improving feature quality.<sup>19–23</sup>

In photolithography,<sup>24–28</sup> the transport properties of the photoacid can change dramatically with changes in the local chemical composition that occur with the deprotection reaction.<sup>24,25</sup> Houle et al. demonstrated that the evolving resist polymer chemistry plays a crucial role in lithographic imaging.<sup>18</sup> An increased photoacid size (the protic acid and neutralizing anion) decreased the apparent diffusion length.<sup>29,30</sup> However, the catalytic efficiency of the acid can dominate, such that by increasing the size of the photoacid conjugate base, image blur occurs primarily due to the local proton mobility, not diffusion of the acid–conjugate base pair.<sup>31,32</sup>

In this paper, the latent chemical image formation during the reaction–diffusion process in a model 193 nm photoresist system, poly(methyladamantyl methacrylate) (PMAAdMA), is measured directly with neutron reflectivity and Fourier transform infrared (FTIR) spectroscopy. An idealized step acid profile is prepared by a sequential spin-coating process (multilayer).<sup>26,33,34</sup> The reaction–diffusion process across this interface occurs during subsequent processing of this ideal optical image. Three ionic photoacid generators are used to measure the reaction front

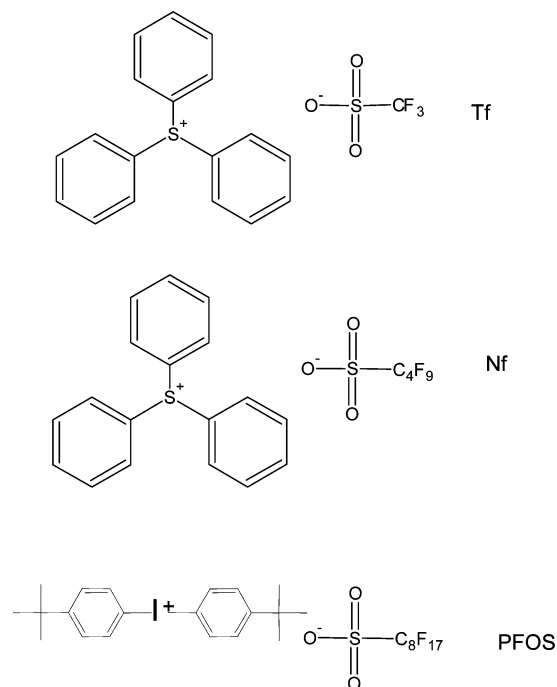
\* To whom correspondence may be addressed. E-mail: vprabhu@nist.gov.

<sup>†</sup> Polymers Division, National Institute of Standards and Technology.

<sup>‡</sup> Center for Neutron Research, National Institute of Standards and Technology.

<sup>§</sup> Sematech.

<sup>||</sup> Certain commercial equipment and materials are identified in this paper in order to specify adequately the experimental procedure. In no case does such identification imply recommendations by the National Institute of Standards and Technology nor does it imply that the material or equipment identified is necessarily the best available for this purpose.

**Scheme 1. Structure of Photoacid Generators (PAGs) Used in This Study<sup>a</sup>**

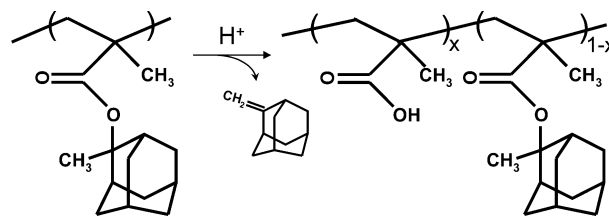
<sup>a</sup> The photoacid size is varied systematically.

profile resulting from different photoacid size. While the extent of propagation is dependent upon the size of the photoacid, as expected, the profile width also changes. Additionally, the influence of the changing chemical composition on the spatial extent of the reaction profile can be clarified. The direct measurement of the reaction–diffusion profile in these experiments provides the insight needed to extend predictive models as well as to select advantageous aspects of this lithographic component. These fundamental measurements are also applicable to improved general understanding of reaction–diffusion processes for applications outside of microelectronics fabrication.

## II. Experimental Section

**A. Materials Characteristics.** Poly(methyladamantyl methacrylate) ( $M_n = 8800$  g/mol, PDI = 1.18) was obtained from DuPont Electronic Materials.<sup>2</sup> PMAdMA films were spin-cast from toluene solution onto silicon wafers (76 mm diameter, 700  $\mu$ m thick) primed with hexamethyldisilazane. The preparation of the bilayer necessitates the formation of a sharp interface between the two layers after spin-coating both layers. The acid-feeder layer examined consists of poly(4-hydroxystyrene) (PHS) (DuPont Electronic Materials,  $M_n = 8000$  g/mol) containing 5% mass fraction of a photoacid generator. Three different PAGs were examined: triphenylsulfonium triflate (TPS-Tf), triphenylsulfonium perfluorobutanesulfonate (TPS-PFBS), and di(*tert*-butylphenyl)iodonium perfluorooctanesulfonate (DTBPI-PFOS). The chemical structures of the PAGs are illustrated in Scheme 1. Vinyl deuterated ( $d_3$ )-PHS (Polymer Source) was used in the acid feeder to determine the partitioning of the methylene adamantane reaction byproduct for some cases.

**B. Sample Preparation.** Details on the preparation of bilayer films are provided elsewhere.<sup>33</sup> Films are postapply baked (PAB) at 130 °C to remove residual solvent. The bilayer is exposed to broadband UV radiation (300 mJ/cm<sup>2</sup>) to activate the PAG. A constant postexposure bake (PEB) temperature of 130 °C is used for the acid-diffusion deprotection reaction. To determine qualitatively the propagation length of the reaction–diffusion process, the acid feeder layer and the deprotected portion of the bottom layer

**Scheme 2. Acid Catalyzed Thermally Activated Deprotection of PMAdMA<sup>a</sup>**

<sup>a</sup> In the presence of acid, the PMAdMA is converted to poly(methacrylic acid) and methylene adamantane.

are developed with aqueous 0.26 N tetramethylammonium hydroxide (TMAH) (Aldrich).

**C. Neutron and X-ray reflectivity.** Neutron reflectivity (NR) measurements were performed at the Center for Neutron Research on the NG-7 reflectometer at the National Institute of Standards and Technology (Gaithersburg, MD) in the following configuration: wavelength ( $\lambda$ ) = 4.768 Å and wavelength spread ( $\Delta\lambda/\lambda$ ) = 0.025. The large difference in hydrogen content between PHS and PMAdMA provides sufficient neutron contrast to allow measurement of the bilayer structure with NR. Further, the hydrogen density of the PMAdMA layer is significantly reduced because of the deprotection reaction product and the loss of methylene adamantane (byproduct), thus providing a route for obtaining the deprotection profile through the film thickness. The physical thickness and surface roughness of the films is measured using X-ray reflectivity.<sup>26</sup>

**D. Fourier Transform Infrared Spectroscopy.** Characterization of the deprotection reaction (see Scheme 2) and methylene adamantane (MA) residual is performed with a Nicolet NEXUS 670 FTIR equipped with a liquid nitrogen cooled MCT/A detector. Double-side polished, with orientation {100} and 1–50  $\Omega$ -cm resistance, silicon wafers were used to minimize substrate absorbance. A wavenumber resolution of 8 cm<sup>-1</sup> was used with averaging over 128 scans to improve the signal-to-noise ratio. The quantification of the deprotection reaction extent is based on the bending vibration mode of CH<sub>3</sub> (1360 cm<sup>-1</sup>) in the protecting MA group of PMAdMA. This band completely disappears and leaves a flat baseline in the IR spectra if all the protected MA groups are reacted. The advantage of choosing this band is that it provides an absolute value of deprotection reaction extent and allows discrimination of the residual MA from the protected PMAdMA group. The quantification of MA residual level is based on the stretching vibration of H–C(=C) (3065 cm<sup>-1</sup>) in the free MA molecule. This band is located at lower wavenumbers than the H–C(–C) vibration (usually <3000 cm<sup>-1</sup>), which makes it possible to quantify the MA content accurately.<sup>35</sup>

The integrated composition of the film determined from FTIR is then used to fit the  $Q_c^2$  profiles obtained from neutron reflectivity; the deprotection level and concentration of methylene adamantane from NR must be consistent with those from FTIR. The composition from FTIR is molar, while the neutron scattering length density is volumetrically based. For comparison purposes, we assume ideal mixing and the specific volume of the components. The density of the PMAdMA and the corresponding fully deprotected polymer are obtained using high-resolution X-ray reflectivity<sup>36</sup> from the critical edge and elemental composition; the relevant parameters are tabulated in Table 1. The use of these molar volumes results in good agreement in the film thickness upon deprotection (within 2 nm) as determined by FTIR and NR measurements. For the FTIR data, the film thickness was determined from the FTIR absorbance calibrated against a fully protected PMAdMA film.

## III. Results

**A. Latent-Image Profiling.** Figure 1a shows neutron reflectivity data for PHS/PMAdMA bilayers containing DTBPI-PFOS in the acid-feeder layer offset as a function of the indicated PEB times at 130 °C. The periodicity of the reflectivity fringe wavelength and amplitude indicates the bilayer structure

**Table 1. Physical Properties of Primary Components**

		PMAdMA	deprotected <sup>a</sup>	methylene adamantane <sup>b</sup>	PHS
density	g/cm <sup>3</sup>	1.13	1.19	0.9	1.23
molar mass	g/mol	233.3	74.1	147.2	120.1
specific vol	cm <sup>3</sup> /mol	206.5	62.3	163.6	97.7
$Q_c^2$ ( $\times 10^{-5}$ )	$\text{\AA}^{-2}$	3.99	5.71	3.15	9.03

<sup>a</sup> To determine the  $Q_c^2$  for fully deprotected PMAdMA, a film of PMAdMA containing 5% TPS–PFBS was exposed and PEB for 5 min at 130 °C. With this processing all the methylene adamantane left the film with 100% deprotection. NR was used to determine the  $Q_c^2$  for this film (Table 1). <sup>b</sup> Estimated density from typical values for substituted liquid adamantanes

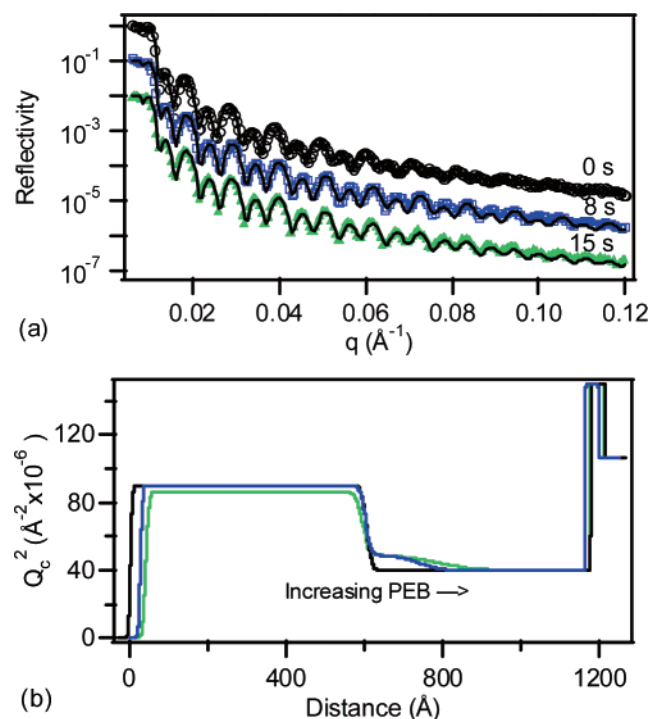


**Figure 1.** (a) Neutron reflectivity profiles for bilayers of PHS (+DTBPI–PFOS) and PMAdMA with (○) 0, (□) 8, and (▲) 30 s PEB at 130 °C. Two distinct beatings are evident in the data due to the NSLD contrast between PHS and PMAdMA. The best fits of the reflectivity are shown by the solid lines corresponding to (b) the NSLD profile. The NSLD of the PMAdMA layer increases with PEB time due to loss of hydrogen content (methylene adamantane).

is composed of layers with distinct scattering length densities. These experimental reflectivity data are fit to reflectivity profiles calculated from model scattering length density profiles ( $Q_c^2 = 16\pi\sum b_i/\nu$ ) using the Parratt algorithm,<sup>37</sup> where the scattering length of each repeat unit is determined by the sum over the atomic scattering lengths  $b_i$  within molar volume ( $\nu$ ) leading to the absolute scattering length density, an intensive absolute quantity. This approach uses successive layers (a box model) of constant  $Q_c^2$  with interfaces smeared by a Gaussian function leading to error function interfacial width profiles.<sup>38</sup> The best fits to the reflectivity data are shown in Figure 1a by the solid lines. The neutron scattering length density profile corresponding to the fit is shown in Figure 1b. The scattering length density profile begins in air at zero, then the scattering length increases to the value of PHS, and then decreases to the value of PMAdMA. The substrate is then encountered with scattering length densities corresponding to the oxide layer ( $\approx 25$  Å thick) and silicon. As PEB time is increased, the  $Q_c^2$  of the MADMA layer near the PHS increases due to the loss of hydrogen content from acid-catalyzed deprotection and the partial volatilization of the methylene adamantane byproduct.

The  $Q_c^2$  profile from Figure 1b cannot be directly interpreted as the deprotection profile due to the presence of residual methylene adamantane after deprotection. This aspect is different from that in a previous study in which the deprotection products were highly volatile with complete outgassing of the reaction products.<sup>26</sup> Therefore, additional experimental data regarding the composition of the film are needed to determine the deprotection profiles from the scattering length density profiles. We provide a description of a general self-consistent scheme that addresses this problem.

In principle, reflectivity data can be fit in terms of the volume fraction profiles ( $\phi_i$ ) of the individual components with a given scattering length density ( $Q_{c,i}^2$ ). For the specific case examined here, we have the following expressions,

$$Q_{c,\text{film}}^2(z) = \phi_{\text{MA}}(z) Q_{c,\text{MA}}^2 + \phi_{\text{MAA}}(z) Q_{c,\text{MAA}}^2 + \phi_{\text{MADMA}}(z) Q_{c,\text{MADMA}}^2$$

$$\phi_{\text{MADMA}}(z) = 1 - \phi_{\text{MA}}(z) - \phi_{\text{MAA}}(z) \quad (1)$$

Since the quantity of deprotection products,  $\phi_{\text{MA}}$ , that remain in the film and the deprotection level designated by  $\phi_{\text{MAA}}$  are unknown, additional information about these two quantities from FTIR measurements are used to fit the NR results. FTIR quantifies the integrated concentrations of MA, MAA, and MADMA within the films through the scheme described previously for both the bilayer and the developed film. These extensive quantities are compared to those calculated from the NR fits as follows,

$$\int dz \phi_{\text{MA}}(z) = N_{\text{MA}}^{\text{NR}}$$

$$\int dz \phi_{\text{MAA}}(z) = N_{\text{MAA}}^{\text{NR}} \quad (2)$$

$N_{\text{MA}}^{\text{NR}}$  is the integrated (extensive quantity) amount per unit area of methylene adamantane that remains in the film and  $N_{\text{MAA}}^{\text{NR}}$  is the integrated degree of deprotection. The component profiles ( $\phi_{\text{MA}}$ ,  $\phi_{\text{MAA}}$ ) are determined using eq 1 by assuming that PMAdMA is completely deprotected at the interface with the acid feeder layer upon PEB and then allowing the deprotection profile to decay smoothly. The decay length is varied to minimize the differences in deprotection and MA amounts between FTIR and NR measurements. Because minimal leaching of the MA in developer is observed, the FTIR on the developed film is compared to the remaining part of the latent profile from NR by changing the limits on the integration in eq 2. For an acceptable fit, the difference between the  $N^{\text{NR}}$  and  $N^{\text{FTIR}}$  is less than 3% for all components. Typically, the least-squares fit of the NR data does not achieve this specification. However, small changes in the scattering length density profile do not significantly affect the quality of the fit. To obtain the best fit, the scattering length density of the deprotected region is changed slightly from the previous fit and only the width and thickness of the deprotection region are allowed to vary. This new  $Q_c^2$  profile is then used to calculate  $N_{\text{MA}}^{\text{NR}}$  and  $N_{\text{MAA}}^{\text{NR}}$  and compared to the FTIR data. This procedure is repeated until the difference between  $N^{\text{NR}}$  and  $N^{\text{FTIR}}$  is less than 3% for all components; typically (1 to 3) iterations are necessary. An example of this procedure is shown in the Supporting Information.

One additional complication arises from the PHS acid feeder layer—this layer could trap some of the residual MA that is measured with FTIR. The MA was determined to reside partially within the PHS and PHS/PMADMA interface by a separate



series of reflectivity experiments using  $d_3$ -PHS that amplify the contrast of the MA. Any accumulation of MA within the deuterated top layer will lower its average scattering length density (SLD); this effect is less pronounced for protonated PHS. A limited concentration (<2 vol % methylene adamantane) is present in the PHS layer with minimal broadening (<10 Å) of the interface between the PHS and PMAdMA during the PEB for the conditions examined. On the basis of the FTIR data, a majority of the methylene adamantane (85–90%) is trapped in the PMAdMA layer. The MA within the PHS layer appears as a slight decrease in the  $Q_c^2$  (Figure 1b) and in the calculation of  $N_{MA}^{NR}$ .

One further possibility that must be examined is the potential segregation of PAG at or away from the interface. DTBPI-PFOS is known to accumulate at the free surface of PHS due to the low surface energy of the fluorinated groups.<sup>39</sup> For the geometry of the bilayer examined in this case, PAG segregation to the free interface will result in a slight decrease in the “bulk” PAG concentration in the film. Thus, the influence of this type of segregation on the measured deprotection front profile will be minor and easily correctable if the free surface concentration profile is known. The segregation of PAG to the polymer–polymer interface would be more problematic in the interpretation of the reaction–diffusion fronts illustrated in this article. For the case of an accumulation of PAG at the buried interface, the initial photoacid concentration would not be a step function. Measurements of the bulk miscibility of PAG in PHS<sup>40</sup> and PMAdMA<sup>41</sup> indicate that the PAG solubility in PHS is significantly greater than in PMAdMA. Thus, thermodynamically, segregation of PAG at this polymer–polymer interface would not be expected, since the PAG is initially added in the more soluble (PHS) phase. For the systems examined here, component segregation artifacts will not influence the interpretation of the result. However, it is important to consider segregation effects when utilizing the bilayer geometry as a model interface for each system examined.

**B. Latent Image: PAG Size Dependence.** Figure 2 shows the deprotection profile determined from the  $Q_c^2$  profiles through the methodology described above. For the largest photoacid (PFOS), the profile for 8 s PEB extends  $\approx 150$  Å into the PMAdMA film with a diffuse profile tail. When the PEB time is increased to 15 s, the reaction front propagates an additional 75 Å, including an increased deprotection level in the tail of the profile. Interestingly, longer PEB times, 30 and 60 s, show greater deprotection extents, but the spatial propagation of the reaction front does not change significantly; only the leading tail increases in deprotection amount. Thus, there exists a limit in the deprotection front propagation with PEB time for the PFOS system. As the PAG size is decreased from DTBPI-PFOS to TPS-PFBS, the width of the deprotection front increases significantly. For TPS-PFBS, the deprotection profile extends completely through the PMAdMA film and continues to propagate as the PEB time increases. Switching to TPS-Tf further increases the reaction extent into the PMAdMA. High deprotection levels extend throughout the film even after only 8 s PEB at 130 °C when using TPS-Tf.

#### IV. Discussion

**Latent Image Profile Features. Influence of Photoacid Generator Size.** The effects of photoacid size on the deprotection profile are shown in Figure 3 for a fixed PEB temperature of 130 °C and time of 8 s. The triflic acid propagates completely through the 600 Å PMAdMA film; deprotecting all of the PMAdMA to extents greater than 40%. The acidic proton does

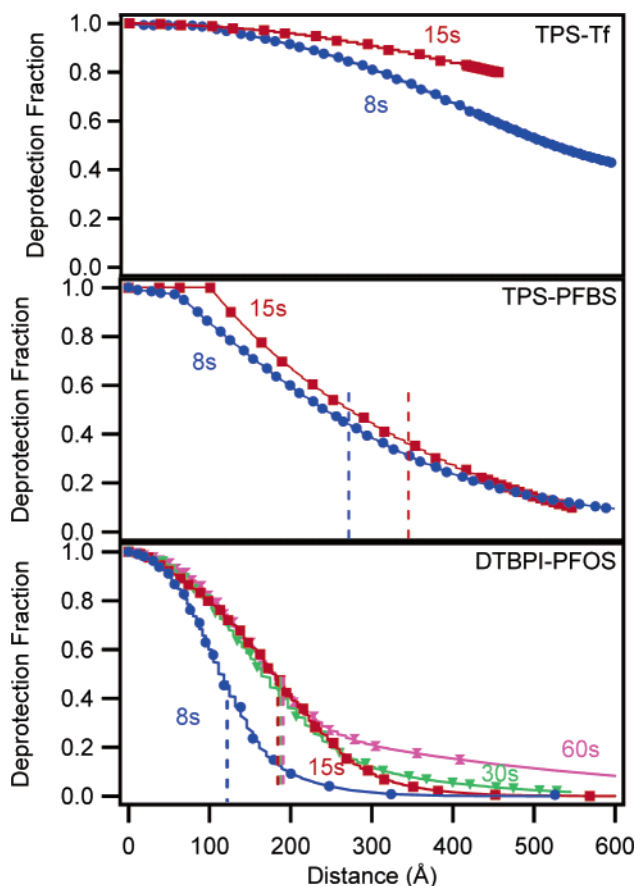


**Figure 2.** Deprotection profiles for different PAGs: TPS-Tf, TPS-PFBS, and DTBPI-PFOS with PEB at 130 °C for (●) 8, (■) 15, (▼) 30, and (hourglass) 60 s. The vertical dashed lines correspond to the developed thickness using 0.26 N TMAH.

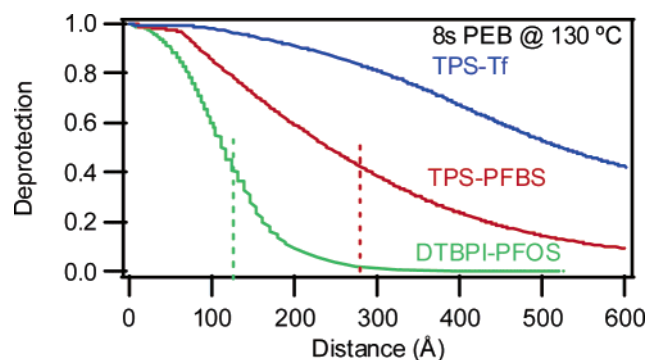


**Figure 3.** Deprotection profiles for model bilayers with 8 s PEB at 130 °C using different PAGs. The dashed lines indicate the solubility switch determined from development with 0.26 N TMAH. As the PAG size increases, the breadth of the deprotection profile decreases. The largest PAG (DTBPI-PFOS) has a much sharper deprotection profile and shorter deprotection propagation in the film compared to the other PAGs.

not diffuse independently, but is coupled to its conjugate base (e.g., triflate, perfluorobutanesulfonate, or perfluorooctanesulfonate). As the photoacid size is increased from Tf to PFBS, the breadth of the reaction front profile narrows and the propagation depth of deprotection decreases. The sharpest latent image profile is found for PFOS. One concern in the direct comparison between different PAGs at a fixed time is interpreting the photoacid diffusive properties because the activation energy for diffusion in these thin films is dependent upon local compositional environment<sup>25</sup> and the PAG itself. However, Hinsberg et al. found no difference in the activation energy for

diffusion between the acid form of Tf and PFBS within a phenolic resist.<sup>24</sup> Thus, we anticipate that observed differences in diffusion between these PAGs are due to the molecular size; not activation energy. It is important to note that the deprotection profiles in Figures 2 and 3 are not photoacid profiles, but represent the image left by the deprotection reaction which follows the reaction kinetics for each photoacid.

From a processing perspective, a larger PAG could be favored because of the smaller diffusion length with equivalent processing—this will limit changes in the critical dimensions and image blur. The shorter diffusion length with increasing PAG size is consistent with previous indirect measurements.<sup>24</sup> Here, the deprotection profile is directly measured using NR with the assistance of FTIR to yield the depth-resolved profile. The importance of this direct measurement is illustrated best by the time evolution of the deprotection profile using DTBPI–PFOS. Although the total deprotection increases with increasing PEB time, the reaction–diffusion of deprotection does not propagate smoothly into the PMAdMA. Previous simulations by others indicate that the reaction–diffusion front propagation rate decreases with increasing PEB time.<sup>24,25</sup> However, a complete arrestment of the front in the highly deprotected region is not predicted from their model.<sup>24,25</sup> For larger PAGs (e.g., PFOS and PFBS), the model predicts profiles at short times (<2 min) to be independent of diffusion; thus, they conclude that reaction kinetics is the important factor in image spreading.<sup>24</sup> However, the measurements here indicate that the PAG size does play an important role even at short times. We note that the simulations are for a different polymer system, so the observed differences in this work could potentially be attributed to chemical composition dependent properties. When examining the measured deprotection profiles for the case of DTBPI–PFOS, initially at short times, the profile follows an error function, as expected by a diffusive process. However at longer times (>15 s), the deprotection front almost ceases to propagate, but instead a tail of low deprotection propagates further into the unreacted region (Figure 2). This behavior is consistent with an acid diffusivity that is strongly dependent upon local chemical environment. The PMAA can interact strongly with ionic species, leading to reduced diffusivity similar to that observed for phenolic resists.<sup>25</sup> The dependence of the diffusivity on the reaction extent is also observed in other reaction–diffusion processes for soft-lithography.<sup>5,9</sup> From a lithographic viewpoint, the arrested front is beneficial because the printed dimensions are not strongly dependent upon small variations in PEB time.

The reaction kinetics for PMAdMA with TPS–PFBS were examined previously.<sup>42</sup> A trapping mechanism of the photoacid with the deprotected product (MAA) was proposed following the work of Houle and co-workers to fit the kinetics data.<sup>25</sup> As mentioned previously, the reaction diffusion front in PMAdMA does not propagate smoothly; there is an arresting of the front at high deprotection extents. This observation is similar to those in model 248 nm photoresists based on PHS.<sup>25</sup> For the case of PHS-based photoresists, the decrease in the diffusivity of the photoacid can be modeled as a reversible reaction between the photoacid and the pendent hydroxyl group of the deprotected monomer.<sup>43</sup> Through a series of papers, researchers at IBM have provided a detailed chemically and physically based model for the reaction diffusion process for a model PHS-based photoresist. These detailed experiments are capable of predicting the shape and extent of the deprotection front for this photoresist material<sup>18,24,25,43–46</sup> as confirmed through direct measurements previously using neutron reflectivity.<sup>26</sup> The switch from hydroxystyrene to methacrylate-based polymers does introduce

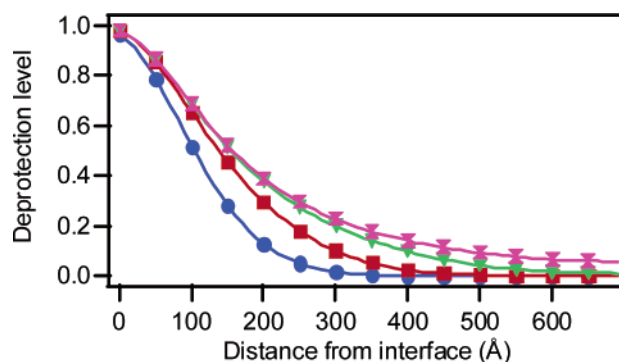


**Figure 4.** Simulated deprotection profiles at a reaction–diffusion front using equations (3) and (4) for PEB of (●) 8 s, (■) 15 s, (▼) 30 s, and (hourglass) 60 s. Similar to Figure 2c, the front is self-limiting and increasing the bake time only increases the background deprotection.

specific effects on the fundamentals of dissolution<sup>47,48</sup> and reaction. For instance the deprotection reaction in PHS is autocatalytic, while methacrylate-based resists generally do not exhibit this characteristic.<sup>49</sup>

On the basis of the initial qualitative interpretation of the reaction diffusion front for PMAdMA, it appears as though the detailed model proposed by Houle and co-workers for PHS<sup>25</sup> also applies to PMAdMA. However, it is unclear if there is a specific binding between the photoacid and the MAA, or there is simply reduced diffusivity in the vicinity of MAA-rich regions. Nonetheless, this mechanism can explain the self-limiting effect of deprotection reaction with PEB time in PAG-loaded PMAdMA films.<sup>42</sup> Here, we apply a simplified scheme to model quantitatively the deprotection profile in a bilayer structure. This model does not include every potential reaction and diffusion step like the IBM model for PHS, and is not meant to serve as an improvement over their model. Instead, this model utilizes a limited number of physically meaningful parameters sufficient to describe the reaction–diffusion process in this system. By including the trapping mechanism into a simple reaction–diffusion model, the following differential equations are derived assuming constant photoacid diffusivity.

$$\frac{d\phi(x,t)}{dt} = k_p(1 - \phi)H(x,t) \quad (3)$$

$$\frac{dH(x,t)}{dt} = D \frac{d^2H(x,t)}{dx^2} - k_T H(x,t)\phi(x,t) \quad (4)$$

where  $\phi(x,t)$  and  $H(x,t)$  are the deprotection level and acid concentration respectively,  $D$  is the diffusion coefficient of the photoacid and  $k_p$  and  $k_T$  are the reaction and the acid trapping rate constants, respectively. We neglect the effect of the residual MA to simplify the modeling. Previously determined rate constants<sup>35</sup> ( $k_p$ ,  $k_T$ ) were used to determine the photoacid diffusion coefficient through the PMAdMA by fitting the deprotection profiles for the bilayers using TPS–PFBS (Figure 2b). Unlike the case of PHS, we find that the photoacid trapping does not need to be modeled as a reversible reaction to describe the data. We speculate that the greater ionizability of the methacrylic acid in comparison to hydroxystyrene leading to stronger binding of the photoacid in the deprotected polymer matrix. Despite the assumptions evoked in eqs 3 and 4, the apparent diffusion coefficient for the photoacid is consistent within a factor of 2 of measurements for PFBS in other fully protected systems,<sup>25</sup> approximately  $6 \times 10^{-13}$  cm<sup>2</sup>/s. Moreover, the self-limiting reaction–diffusion front can be qualitatively predicted by eqs 3 and 4. Figure 4 shows the simulated profiles

using reasonable parameters for a slow, strong photoacid ( $k_p = 30 \text{ nm}^3/\text{s}$ ;  $k_T = 0.4 \text{ nm}^3/\text{s}$ ;  $D = 1 \times 10^{-13} \text{ cm}^2/\text{s}$ ). Although it is possible to fit the data in Figure 2c, which shows a self-limiting front, we did not perform this curve fitting routine because  $k_p$  and  $k_T$  have not been independently determined for PFOS. As such, the extracted diffusivity would be unreliable. However, the simulated data in Figure 4 qualitatively predict the data shown in Figure 2c. The model of Houle et al. was not used for these data sets of the reaction diffusion front profiles due to limitations in independently determining the physical parameters needed in the model. The simplified model utilized here is useful for estimating reaction–diffusion processes in cases where detailed knowledge of the reaction–diffusion processes is limited.

Arrestment of the reaction front propagation is accurately depicted by deprotection products trapping the photoacid. This result suggests that the diffusivity of the photoacid varies linearly with the deprotection concentration, since the trapping was assumed to be a first-order reaction. However, this model could be utilized to describe systems with a more complex diffusivity dependence on reactant concentration through modification of the reaction order. When there are large disparities in the diffusivity upon reaction, this trapping reaction approach appears to be a robust method to model reaction–diffusion without fully solving a variable diffusion coefficient problem. A similar modeling approach may be applicable to simplifying other reaction diffusion problems.

The methodology presented here may be useful in understanding localization behavior in reaction–diffusion. The methods are generalized such that neutron reflectivity should be able to elucidate details of the reaction–diffusion process with sub-nm precision. The use of a complementary technique such as FTIR in combination with reflectivity allows for improved confidence in the interpretation of the neutron reflectivity profile, compensating for the nonunique solution due to the loss of phase information. The high-resolution measurement of the reaction–diffusion front is important to fully realizing the potential of reaction–diffusion processes outside of the microelectronics industry.

**B. Development of Latent Image.** The bilayer structures can be partially dissolved in aqueous hydroxide solution to reveal the model line-edge. During this process, the top PHS layer is completely dissolved as well as a fraction of the underlying deprotection profile in 0.26 N TMAH. Despite the broad deprotection profile, the developed film generally has a smooth surface as previously observed by Lin et al.<sup>26</sup> The partial development of these films is complex because the solubility is controlled by the methacrylic acid comonomer content. Additionally, the large fraction of hydrophobic methylene adamantane that remains within the film must also be considered with regards to the influence on the final feature quality.

The vertical dashed lines in Figures 2 and 3 are the final film thickness determined by X-ray reflectivity. The bilayer film develops into the latent-image profile until an average deprotection level of less than approximately 40% is reached when using 0.26 N TMAH. After development, FTIR measurements show that MA remains within the film and the average deprotection levels interpreted by NR remain consistent with FTIR. The MA in the nondissolved portion of the bilayer does not leach out during development.

The change in dimension of the PMAdMA is strongly PAG dependent due to the differences in deprotection profiles (Figure 3). No film remains in the bilayers using Tf even after only 8 s PEB at 130 °C. Using PFBS results in a continual decrease in

the PMAdMA film thickness with increasing PEB time up to 30 s where nearly all the film is dissolved. The observed behavior of the PFOS is quite different; initially with 8 and 15 s PEB there is a decrease in the remaining film thickness. However increasing the PEB time to 30 or 60 s does not substantially increase the quantity of PMAdMA dissolved. This behavior is consistent with the deprotection profiles obtained from NR (Figure 2). The necessary deprotection for these films to dissolve is approximately 40%. Thus, the solubility switch for the PMAdMA is independent of the photoacid and PEB time as expected. The sensitivity of the composition gradient to the choice of PAG is illustrated in these results. The half-width of the deprotection gradient is nearly five times greater when using PFBS than PFOS. Many of the final developed feature properties are related to the width of the deprotection profile.<sup>18,19,46</sup> Additionally, the deprotection front profile for the PFBS and Tf bilayers can be used to estimate the acid diffusion length.<sup>24</sup> The diffusion length difference between the PFBS and Tf is approximately a factor of 2, consistent with volumetric difference between PFBS and Tf.

## V. Conclusions

The depth-resolved deprotection profile of a model 193 nm photoresist was measured by combining neutron reflectivity and infrared spectroscopy as a function of photoacid generator size. The larger the photoacid, the shorter the deprotection depth into the PMAdMA film and the sharper the deprotection profile. In the case of the largest PAG used, the reaction–diffusion front at long time is characterized by a virtual stop in the highly deprotected region and further reaction–diffusion occurs only by extending the reaction front of low level deprotection into the unreacted region. This observation supports the notion that the photoacid mobility depends strongly on the local composition of the photoresist; it decreases dramatically in regions containing mostly deprotected species. A simple reaction and diffusion-trapping model provides an adequate description of the experimentally observed shape with the self-limiting reaction–diffusion front. These direct measurements of the profile shapes and the diffusion trapping model provide the necessary fundamentals to understand lithographic imaging.

**Acknowledgment.** This work was supported by SEMATECH under Agreement No. 309841 OF. The authors acknowledge Drs. Jim Sounik and Michael Sheehan at DuPont Electronic Polymers for providing the polymers used in this study.

**Supporting Information Available:** Text giving additional details and example of self-consistent fit methodology by combining neutron reflectivity and FTIR reaction front data for PMAdMA/PHS and d3-PHS and bilayers, a table of scattering length density, and figures showing the influence of deuteration on the reflectivity profile and subsequent fits and fits of the reflectivity data. This material is available free of charge via the Internet at <http://pubs.acs.org>.

## References and Notes

- (1) Sachs, C.; Hildebrand, M.; Volkening, S.; Winterlin, J.; Ertl, G. *Science* **2001**, 293 (5535), 1635–1638.
- (2) Newman, E. A.; Zahs, K. R. *Science* **1997**, 275 (5301), 844–847.
- (3) Ouyang, Q.; Swinney, H. L. *Nature (London)* **1991**, 352 (6336), 610–612.
- (4) Kauffman, S. A.; Shymko, R. M.; Trabert, K. *Science* **1978**, 199 (4326), 259–270.
- (5) Grzybowski, B. A.; Bishop, K. J. M.; Campbell, C. J.; Fialkowski, M.; Smoukov, S. K. *Soft Matter* **2005**, 1 (2), 114–128.
- (6) Liesegang, R. E. *Naturwiss. Wochenschr.* **1896**, 11, 353–362.



- (7) Henisch, H. *Crystals in Gels and Liesegang Rings*; Cambridge University Press: Cambridge, U.K., 1998.
- (8) Turing, A. M. *Philos. Trans. R. Soc. London, Ser. B—Biol. Sci.* **1952**, 237, 37.
- (9) Campbell, C. J.; Fialkowski, M.; Klajn, R.; Bensemann, I. T.; Grzybowski, B. A. *Adv. Mater.* **2004**, 16, 1912.
- (10) Campbell, C. J.; Smoukov, S. K.; Bishop, K. J. M.; Grzybowski, B. A. *Langmuir* **2005**, 21, 2637–2640.
- (11) Holloway, K.; Fryer, P. M.; Cabral, C.; Harper, J. M. E.; Bailey, P. J.; Kelleher, K. H. *J. Appl. Phys.* **1992**, 71, 5433–5444.
- (12) Hinsberg, W.; Houle, F. A.; Hoffnagle, J.; Sanchez, M.; Wallraff, G.; Morrison, M.; Frank, S. *J. Vac. Sci. Technol. B* **1998**, 16, 3689–3694.
- (13) Pawloski, A.; Acheta, A.; Lalovic, I.; LaFontaine, B.; Levinson, H. *Proc. SPIE, Adv. Resist Technol. Process. XXI* **2004**, 5376, 414.
- (14) Ito, H. *J. Polym. Sci., Part A: Polym. Chem.* **2003**, 41, 3863–3870.
- (15) Willson, C.; Ito, H.; Frechet, J.; Tessier, T.; Houlihan, F. *J. Electrochem. Soc.* **1986**, 133 (1), 181–187.
- (16) Ito, H. *Adv. Polym. Sci.* **2005**, 172, 37–245.
- (17) Wallraff, G. M.; Hinsberg, W. D. *Chem. Rev.* **1999**, 99, 1801–1821.
- (18) Houle, F. A.; Hinsberg, W. D.; Sanchez, M. I.; Hoffnagle, J. A. *J. Vac. Sci. Technol. B* **2002**, 20, 924–931.
- (19) Kim, J. H.; Kim, Y. H.; Chon, S. M.; Nagai, T.; Noda, M.; Yamaguchi, Y.; Makita, Y.; Nemoto, H. *J. Photopolym. Sci. Technol.* **2004**, 17, 379–384.
- (20) Schmid, G. M.; Stewart, M. D.; Singh, V. K.; Willson, C. G. *J. Vac. Sci. Technol. B* **2002**, 20, 185–190.
- (21) Stewart, M. D.; Tran, H. V.; Schmid, G. M.; Stachowiak, T. B.; Becker, D. J.; Willson, C. G. *J. Vac. Sci. Technol. B* **2002**, 20, 2946–2952.
- (22) Hoffnagle, J. A.; Hinsberg, W. D.; Sanchez, M. I.; Houle, F. A. *Opt. Lett.* **2002**, 27 (20), 1776–1778.
- (23) *International Technology Road map for Semiconductors*; 2004 Update; 04.
- (24) Hinsberg, W. D.; Houle, F. A.; Sanchez, M. I.; Wallraff, G. M. *IBM J. Res. Dev.* **2001**, 45, 667–682.
- (25) Houle, F. A.; Hinsberg, W. D.; Morrison, M.; Sanchez, M. I.; Wallraff, G.; Larson, C.; Hoffnagle, J. *J. Vac. Sci. Technol. B* **2000**, 18, 1874–1885.
- (26) Lin, E. K.; Soles, C. L.; Goldfarb, D. L.; Trinquet, B. C.; Burns, S. D.; Jones, R. L.; Lenhart, J. L.; Angelopoulos, M.; Willson, C. G.; Satija, S. K.; Wu, W. L. *Science* **2002**, 297, 372–375.
- (27) Schlegel, L.; Ueno, T.; Hayashi, N.; Iwayanagi, T. *J. Vac. Sci. Technol. B* **1991**, 9, 278–289.
- (28) Zuniga, M.; Wallraff, G. M.; Neureuther, A. R. *Proc. SPIE—Int. Soc. Opt. Eng.* **1995**, 2438, 113–124.
- (29) Croffie, E.; Yuan, L.; Cheng, M. S.; Neureuther, A.; Houlihan, F.; Cirelli, R.; Watson, P.; Nalamasu, O.; Gabor, A. *J. Vac. Sci. Technol. B* **2000**, 18, 3340–3344.
- (30) Itani, T.; Yoshino, H.; Fujimoto, M.; Kasama, K. *J. Vac. Sci. Technol. B* **1995**, 13, 3026–3029.
- (31) Resibois, P. *Electrolyte theory; an elementary introduction to a microscopic approach*; Harper & Row: New York, 1968.
- (32) Shi, X. L. *J. Vac. Sci. Technol. B* **1999**, 17, 350–354.
- (33) Jones, R. L.; Prabhu, V. M.; Goldfarb, D. L.; Lin, E. K.; Soles, C. L.; Lenhart, J. L.; Wu, W. L.; Angelopoulos, M. *Correlation of the reaction front with roughness in chemically amplified photoresists*; ACS Symposium Series 874; American Chemical Society: Washington, DC, 2004; pp 86–97.
- (34) Goldfarb, D. L.; Angelopoulos, M.; Lin, E. K.; Jones, R. L.; Soles, C. L.; Lenhart, J. L.; Wu, W. L. *J. Vac. Sci. Technol. B* **2001**, 19, 2699–2704.
- (35) Kang, S. H.; Prabhu, V. M.; Vogt, B. D.; Lin, E. K.; Wu, W. L.; Turnquest, K. *Polymer* **2006**, 47, 6293–6302.
- (36) Lee, H.-J.; Lin, E. K.; Bauer, B. J.; Wu, W.; Hwang, B. K.; Gray, W. D. *Appl. Physics Lett.* **2003**, 82, 1084–1086.
- (37) Parratt, L. G. *Phys. Rev.* **1954**, 95, 359–369.
- (38) Russell, T. P. *Mater. Sci. Rep.* **1990**, 5, 171–271.
- (39) Lenhart, J. L.; Jones, R. L.; Lin, E. K.; Soles, C. L.; Wu, W.; Fischer, D. A.; Sambasivan, S.; Goldfarb, D. L.; Angelopoulos, M. *J. Vac. Sci. Technol. B* **2002**, 20, 2920–2926.
- (40) VanderHart, D. L.; Prabhu, V. M.; Lin, E. K. *Chem. Mater.* **2004**, 16, 3074–3084.
- (41) VanderHart, D. L. Unpublished Work, 2006.
- (42) Kang, S.; Prabhu, V. M.; Vogt, B. D.; Lin, E. K.; Wu, W. L.; Turnquest, K. *Proc. SPIE—Int. Soc. Opt. Eng.* **2006**, 6153, 61533N.
- (43) Wallraff, G.; Hutchinson, J.; Hinsberg, W.; Houle, F.; Seidel, P.; Johnson, R.; Oldham, W. *J. Vac. Sci. Technol. B* **1994**, 12, 3857–3862.
- (44) Hinsberg, W.; Wallraff, G.; Houle, F.; Morrison, M.; Frommer, J.; Beyers, R.; Hutchinson, J. *Org. Thin Films* **1998**, 695, 344–359.
- (45) Hinsberg, W.; Houle, F.; Sanchez, M.; Morrison, M.; Wallraff, G.; Larson, C.; Hoffnagle, J.; Brock, P.; Breyta, G. *Proc. SPIE—Int. Soc. Opt. Eng.* **2000**, 3999, 148–160.
- (46) Houle, F. A.; Hinsberg, W. D.; Sanchez, M. I. *J. Vac. Sci. Technol. B* **2004**, 22, 747–757.
- (47) Hinsberg, W.; Houle, F. A.; Lee, S. W.; Ito, H.; Kanazawa, K. *Macromolecules* **2005**, 38, 1882–1898.
- (48) Ito, H.; Fenzel-Alexander, D.; Breyta, G. *Proc. SPIE—Int. Soc. Opt. Eng.* **1997**, 3049, 575–584.
- (49) Paniez, P. J.; Gally, S.; Mortini, B. P.; Rosilio, C.; Sassoulas, P.-O.; Dammel, R. R.; Padmanaban, M.; Klauck-Jacobs, A.; Oberlander, J. E. *Proc. SPIE—Int. Soc. Opt. Eng.* **1999**, 3678, 1352–1363.

MA061209L